



Contents lists available at ScienceDirect

## International Journal of Mechanical Sciences

journal homepage: [www.elsevier.com/locate/ijmecsci](http://www.elsevier.com/locate/ijmecsci)

# Acoustic multi-stopband metamaterial plates design for broadband elastic wave absorption and vibration suppression



Hao Peng\*, P. Frank Pai, Haoguang Deng

Department of Mechanical and Aerospace Engineering, University of Missouri, Columbia, MO 65211, USA

## ARTICLE INFO

## Article history:

Received 23 January 2015

Received in revised form

21 August 2015

Accepted 26 August 2015

Available online 11 September 2015

## Keywords:

Acoustic metamaterial plate

Multi-stopband

Vibration absorber

Dispersion

## ABSTRACT

This paper presents the modeling technique, working mechanism and design guidelines for acoustic multi-stopband metamaterial plates for broadband elastic wave absorption and vibration suppression. The metamaterial plate is designed by integrating two-degree of freedom (DOF) mass–spring subsystems with an isotropic plate to act as vibration absorbers. For an infinite metamaterial plate without damping, a working unit is modeled using the extended Hamilton's principle, and two stopbands are observed through dispersion analysis on the averaged three-DOF model. For a finite metamaterial plate with boundary conditions and damping, shear-deformable conforming plate elements are used to model the whole plate, and stopbands are investigated by frequency response analysis and transient analysis. Influences of absorbers' resonant frequencies and damping ratios, plate's boundary conditions and dimensions, and effective plate-absorber vibration modes are thoroughly investigated. Results show that the metamaterial plate is essentially based on the concept of conventional vibration absorbers. The local resonance of the two-DOF subsystems generates two stopbands, and the inertial forces generated by the resonant vibrations of absorbers straighten the plate and attenuate/stop wave propagation. Each stopband's bandwidth can be increased by increasing the absorber mass and/or reducing the average mass of isotropic plate in each working unit. Moreover, while a low damping ratio for the primary absorber can guarantee absorbers' quick response to transient excitations, a high damping ratio for the secondary absorber can combine the two stopbands into a wide one. In the end, a sensitivity analysis on absorber resonant frequencies is conducted and relatively large sensitivity is found at the two stopband regions.

© 2015 Elsevier Ltd. All rights reserved.

## 1. Introduction

The concept of metamaterials was first discussed in 1968 [1] but most of the early studies focused on electromagnetic metamaterials (EMs), which are materials with negative permittivity and permeability. Famous properties of EMs include negative refractive indices [2], ability of invisibility [3,4], and inverse Doppler effect [5]. Based on the similarity between electromagnetic waves and acoustic waves, a new type of metamaterials called acoustic metamaterials was proposed and investigated in recent years [6–10]. Popular research topics about acoustic metamaterials include ultrasound focusing [11], acoustic cloaking [12], elastic wave absorption [13] and structural vibration mitigation [14]. Because earthquake often generates destructive body and surface waves [15], seismic waveguides are an important application of acoustic metamaterials. For example, Kim and Das proposed a novel seismic attenuator made of metamaterials based on the characteristics of different seismic waves [16], and Brule et al. [17]

experimentally investigated seismic metamaterials interaction with seismic waves by molding the surface waves.

Phononic crystals (PCs), sometimes also classified as a special kind of acoustic metamaterials by some researchers [18,19], have been under investigation since the 1990s [20–22]. Similar to acoustic metamaterials, PCs usually exhibit anomaly properties, such as stopbands (or bandgaps) [23], negative refractive index [24] and Fano profiles [25], but the difference between PCs and acoustic metamaterials is also significant. Detailed comparison between acoustic metamaterials and PCs have been done by lots of researchers [6,18,19]. PCs, analogous to the idea of photonic crystals, are artificial composite materials consisting of acoustic functional scatters of high impedance and matrix of low impedance. Because PCs are based on the idea of *Bragg scattering*, the scatters must be arranged spatially on the order of the matrix acoustic wavelength [6]. However, wavelengths of environmental low-frequency sound waves are usually large and hence absorption of such waves requires large size PCs, which usually limits the application [26]. One solution to this problem is to use acoustic metamaterials.

\* Corresponding author. Tel.: +1 209 600 8498.

Instead of relying on Bragg scattering effect, acoustic metamaterials utilize local resonance of inclusions, and hence the size of acoustic metamaterials can be far less than the wavelength. For example, the acoustic metamaterials proposed in 2000, consisting of rubber-coated lead balls, are two orders smaller than the incident wavelength [27]. Acoustic metamaterials can be further classified into *intrinsic* and *inertial* ones [6]. In intrinsic acoustic metamaterials, the phase speed of the inclusions (e.g., soft silicon rubber [28]) is much lower than that of the matrix [29,30]. Instead of requiring inclusions with low phase velocity, inertial acoustic metamaterials employ mass–spring–damper subsystems as local resonators. The inertial forces of the subsystems under resonance work against the excitation and attenuate the vibration. Early studies on inertial acoustic metamaterials focused on dispersion analysis and band structures of mass–spring lattice systems. For example, In 2003 phononic stopbands of 1-D and 2-D mass–spring lattice structures with two types of working units were extensively investigated [31]. Subsequently, different types of mechanical lattice structures with stopbands were proposed [32]. The effect of attaching mass–spring subsystems to a rigid body was investigated in 2007 [33]. In 2008 the negative effective mass and stopbands of a 1D mass–spring system was experimentally verified [34]. The experiment was conducted on an air track and CCD cameras were used to capture the motion of the masses.

Although inertial acoustic metamaterials with lattice structures have been widely discussed, metamaterials with continuum structures like bars, beams, plates and shells, which are more commonly used in engineering designs, have not been fully studied. In 2008 Cheng et al. [35] proposed a 1-D ultrasonic metamaterial beam showing simultaneously negative dynamic density and modulus. The metamaterial beam was constructed by attaching Helmholtz resonators to an elastic beam, and analyzed with an acoustic transmission line method. The results was confirmed by finite-element analysis using solid elements for both the elastic beam and the Helmholtz resonators. The model was latter improved with parallel-coupled Helmholtz resonators [36]. In 2008 and 2010 Wu [37] and Oudich [38] proposed metamaterial plates with periodic stubbed surface. Both of them reported stopbands in metamaterials either using single-material stubs with height three times the plate thickness, or using rubber stubs with metal caps. No matter the metamaterials are constructed by rubber-coated lead balls [27], Helmholtz resonators [35,36], or plates with stubbed surface [37,38], all the local resonators can be modeled by simple mass–spring subsystems. However, due to difficulties in modeling local deformation/motion of discrete mass–spring subsystems attached to continuum bodies by classical continuum theories, such models have not been well analyzed [39]. Zhu et al. [39] proposed a microstructure continuum model to tackle the problem but the displacement in the continuum body was approximated by linear series expansions in terms of quantities defined at the cell center, rather than modeled with classical continuum theory. A review of previous elastic metamaterial plates have been done by Zhu et al. [40].

Based on the classical continuum theory [41], we have done extensive work on metamaterial bars, beams and plates by modeling the discrete local resonators as essential mass–spring subsystems [7–10]. In 2010 a metamaterial bar made of a hollow longitudinal bar with mass–spring subsystems attached inside was introduced [7]. Dispersion analysis and finite-element modeling showed that a stopband was created by the subsystems, and the stopband was tunable by changing the resonant frequencies of the subsystems. Following a similar approach, a metamaterial beam was designed by attaching translational and rotational subsystems to an elastic beam [9]. Timoshenko's beam theory and rotary inertias were included in the model because shear deformation and rotary inertias are important for thick beams and/or high-

frequency vibrations. Finite-element analysis showed a tunable stopband and the attached rotational inertias were proved to be not as efficient as the translational inertias. In 2014 the stopband is largely expanded by introducing a multi-stopband metamaterial beams. Two stopband are connected into a wide one by attaching a secondary vibration absorber to the primary one and applying large damping to the secondary vibration absorber [8]. Recently Peng and Pai [10] proposed metamaterial plates with mass–spring subsystems for wave absorption and vibration suppression.

Metamaterial plates have more engineering applications than metamaterial bars or beams. For example, metamaterial plates can be used to protect important building structures (e.g., museums, dams and school buildings) during earthquakes and reduce noise in residential halls. To the authors' knowledge, metamaterial plate models based on the idea of multi-frequency mass–spring absorbers have never been presented in the literatures. This paper is aimed to design a multi-stopband metamaterial plate for broadband vibration absorption by employing the local resonance between the multi-frequency absorbers and the external excitation. Each absorber consists of a primary and a secondary absorber and hence the multiple resonant frequencies of the subsystems can be used to attenuate/stop broadband elastic waves. Guidelines for appropriate design of primary and secondary absorbers are derived. Influences of absorbers' resonant frequencies and damping ratios, plate's boundary conditions and dimensions, and acoustic and optical plate-absorber vibration modes are fully investigated.

## 2. Multi-frequency vibration absorber

A single stopband exists right above the resonant frequency of a conventional single-mass vibration absorber [7,42]. Increase of the absorber damping can widen the stopband to some degree, but the effect is minimal. Moreover, large absorber damping slows down the absorber's response to an excitation and increases the transient time. These shortcomings of conventional vibration absorbers prompt the idea of using multi-frequency vibration absorbers. Fig. 1 shows a multi-frequency vibration absorber. The base system  $m$  is connected to the ground by the spring  $k$  and the damper  $c$  and subjected to a harmonic excitation  $f$  with an amplitude  $f_0$  and a frequency  $\omega$ . The displacement of the base system is denoted by  $u$ . Different from the conventional vibration absorber, two masses  $m_1$  and  $m_2$ , instead of a single mass, are attached to the base system. The displacements of the primary and secondary masses are denoted by  $u_1$  and  $u_2$ , respectively. This multiple-frequency vibration absorber is designed such that the

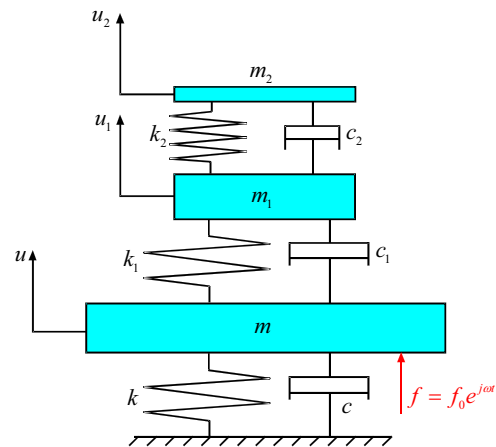


Fig. 1. A multi-frequency vibration absorber.

primary vibration absorber can quickly respond to the base system's vibration while the secondary vibration absorber can significantly damp out the vibration energy transferred into the absorbers by using a high damping value for  $c_2$ . According to Newton's second law, the equation of motion for this 3-DOF system can be obtained as

$$[M]\{\ddot{d}\} + [C]\{\dot{d}\} + [K]\{d\} = \{F\} \quad (1)$$

where

$$[M] = \begin{bmatrix} m & 0 & 0 \\ 0 & m_1 & 0 \\ 0 & 0 & m_2 \end{bmatrix}, \quad \{d\} = \begin{Bmatrix} u \\ u_1 \\ u_2 \end{Bmatrix}$$

$$[C] = \begin{bmatrix} c+c_1 & -c_1 & 0 \\ -c_1 & c_1+c_2 & -c_2 \\ 0 & -c_2 & c_2 \end{bmatrix},$$

$$[K] = \begin{bmatrix} k+k_1 & -k_1 & 0 \\ -k_1 & k_1+k_2 & -k_2 \\ 0 & -k_2 & k_2 \end{bmatrix}, \quad \{F\} = \begin{Bmatrix} f \\ 0 \\ 0 \end{Bmatrix} \quad (2)$$

For frequency response analysis (FRA), the system is subjected to a harmonic excitation

$$\{F\} = \{F_0\}e^{j\omega t} \quad (3)$$

and the frequency response function matrix  $[H]$  is given by

$$\{d_0\} = [H]\{F_0\}, [H] \equiv (-\omega^2[M] + j\omega[C] + [K])^{-1} \quad (4)$$

where  $\{d_0\}$  is the steady-state vibration amplitude vector of the three masses,  $[H]$  contains frequency response functions (FRFs),  $\{F_0\} = \{f_0, 0, 0\}^T$  and  $j \equiv \sqrt{-1}$ . The frequency response functions for  $m$ ,  $m_1$  and  $m_2$  are  $|H_{11}|$ ,  $|H_{21}|$  and  $|H_{31}|$ , respectively. Because the model in Fig. 1 is a 3-DOF system, three response peaks are expected in each FRF, and hence there are two low-response frequency bands among the three peaks, as shown later in Fig. 3(a). These two low-response frequency bands can be regarded as stopbands of the 3-DOF system. Two local resonant frequencies of the absorber are defined as  $\omega_{n1} \equiv \sqrt{k_1/m_1}$  and  $\omega_{n2} \equiv \sqrt{k_2/m_2}$ . The working principle of the vibration absorber is to make  $u=0$  by adjusting one of these two local resonant frequencies equal to the excitation frequency  $\omega$ . If there is no damping in the system (i.e.,  $c=c_1=c_2=0$ ), the two zero-response frequencies  $\omega_i$  can be derived from Eqs. (2) and (4) to be

$$\omega_1, \omega_2 = \omega_{n1} \sqrt{\frac{r+rs+s \pm \sqrt{(r+rs+s)^2 - 4rs}}{2r}} \quad (5)$$

where  $r \equiv m_2/m_1$  and  $s \equiv k_2/k_1$ . If  $r$  is fixed to be 0.03, 0.05 and 0.08, respectively, Fig. 2(a) depicts how  $\omega_i$  changes with  $s$ . Note that both  $\omega_1$  and  $\omega_2$  increase when  $r$  decreases and/or  $s$  increases. Because the design purpose is to eliminate the middle response peak and combine the two low-response frequency bands into one, a narrow bandwidth between  $\omega_1$  and  $\omega_2$  is desired. The broken lines in Fig. 2(a) and (b) show that  $\omega_2 - \omega_1$  reaches its minimum when  $r=s$ , and  $\omega_2 - \omega_1$  decreases when  $r(=s)$  decreases. This is a very valuable design guideline.

For numerical simulations,  $r=s$  is used by following the previous reasoning and the parameters of the 3-DOF system are chosen to be

$$m = 10 \text{ kg}, \quad m_1 = 1 \text{ kg}, \quad m_2 = rm_1, \quad k_2 = sk_1, \quad r=s, \quad \zeta_i \equiv c_i/(2m_i\omega_{ni})$$

$$\omega_n = \sqrt{k/m} = 10 \text{ Hz}, \quad \omega_{n1} = \sqrt{k_1/m_1} = 10 \text{ Hz}, \quad \omega_{n2} = \sqrt{k_2/m_2} = 10 \text{ Hz}$$

First, the three damping ratios are set to be  $\zeta = \zeta_1 = \zeta_2 = 0.02$  and the mass ratio  $r$  is varied. Fig. 3 shows the FRFs of  $m$ ,  $m_1$  and  $m_2$  under different  $r(=s)$  values. The black dash line in Fig. 3

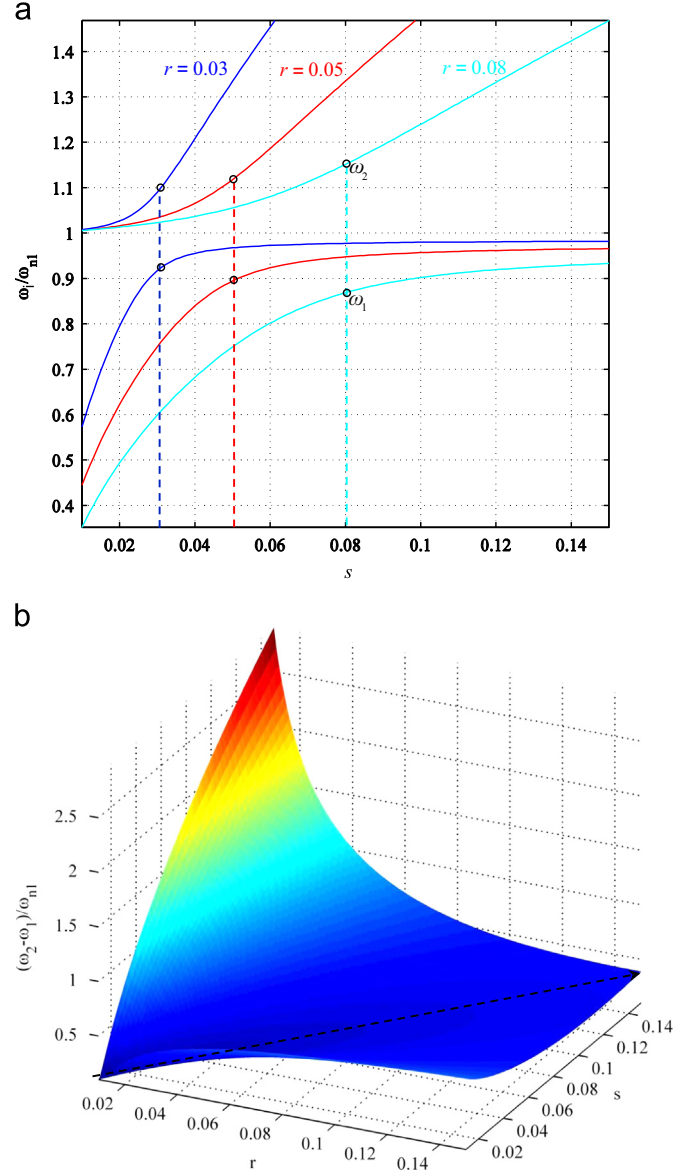
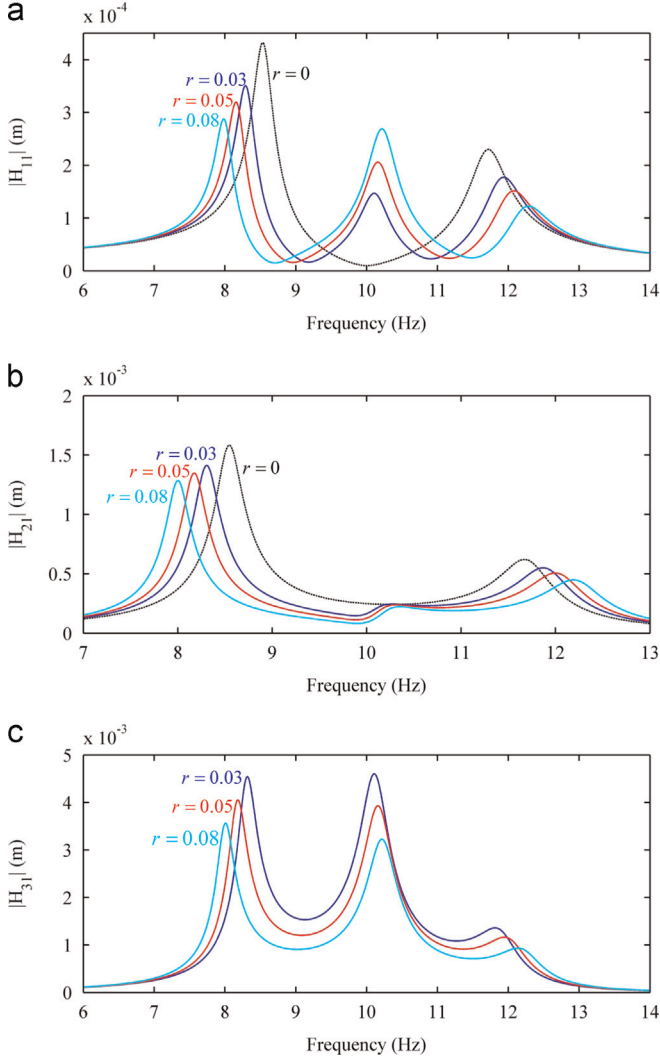


Fig. 2. Variation of zero-response frequencies  $\omega_i$  with  $r$  and  $s$ : (a)  $\omega_1$  and  $\omega_2$ , and (b)  $\omega_2 - \omega_1$ .

(a) shows that if  $r=0$  (i.e., the system becomes a 2-DOF system), there are only two response peaks and the single zero-response frequency is 10 Hz. If  $r>0$ , there are two zero-response frequencies  $\omega_1$  and  $\omega_2$ , which are located at left and right sides of  $\omega_{n1} = 10$  Hz and  $(\omega_1 + \omega_2)/2 \approx \omega_{n1}$ . Fig. 3(a) shows that, when  $r$  increases,  $\omega_2 - \omega_1$  increases and the middle response peak increases. Hence, it becomes more difficult to eliminate the middle response peak and combine the two low-response bands around  $\omega_1$  and  $\omega_2$  into one large low-response frequency band when  $r$  is large. Fig. 4 shows how the middle response peak of  $u$  is eliminated by choosing appropriate values for  $r(=s)$  and  $\zeta_2$ . With  $\zeta = \zeta_1 = 0.02$ , Fig. 4(a) shows that  $\zeta_2 = 0.1$  successfully eliminates the middle response peak for cases with  $r=0.03$  and 0.05 but does not work for cases with  $r=0.08$  and 0.12. In Fig. 4(c),  $\zeta = \zeta_1 = 0.02$  and  $r=0.05$  are used and  $\zeta_2$  varies from 0.02 to 0.15. The middle response peak is eliminated if  $\zeta_2$  is higher than 0.1. Hence, another design guideline derived from these results is that an optimal set of values for  $r(=s)$  and  $\zeta_2$  is needed in order to eliminate the middle response peak and expand the low-response frequency band.



**Fig. 3.** FRFs under  $\zeta = \zeta_1 = \zeta_2 = 0.02$  and different  $r (=s)$  values: (a) FRFs of  $m$ , (b) FRFs of  $m_1$ , and (c) FRFs of  $m_2$ .

### 3. Dispersion analysis of multi-stopband metamaterial plate

The previous section analyzed a 3-DOF multi-frequency vibration absorber composed of three parts: the base structure ( $m$ ), the primary vibration absorber ( $m_1$ ) and the secondary vibration absorber ( $m_2$ ). Based on this 3-DOF multi-frequency vibration absorber, a working unit of a multi-stopband metamaterial plate is created by replacing the base structure  $m$  with an isotropic rectangular plate as shown in Fig. 5a, where the Cartesian coordinate system is defined with its origin at the center of the plate and the plate dimensions are  $2a \times 2b \times h$ . First we define momentum resultants  $M_1$ ,  $M_2$  and  $M_6$  as [41]

$$\begin{aligned} M_1 &= \int_{-h/2}^{h/2} \sigma_{11} z dz = -D(w_{xx} + \nu w_{yy}), \\ M_2 &= \int_{-h/2}^{h/2} \sigma_{22} z dz = -D(\nu w_{xx} + w_{yy}), \\ M_6 &= \int_{-h/2}^{h/2} \sigma_{12} z dz = -D(1-\nu)w_{xy}, \\ D &\equiv \frac{Eh^3}{12(1-\nu^2)} \end{aligned} \quad (6)$$

where  $\sigma_{11}$  and  $\sigma_{22}$  are normal stresses along the  $x$  and  $y$  directions,  $\sigma_{12}$  is the in-plane shear stress and  $w$  is the vertical

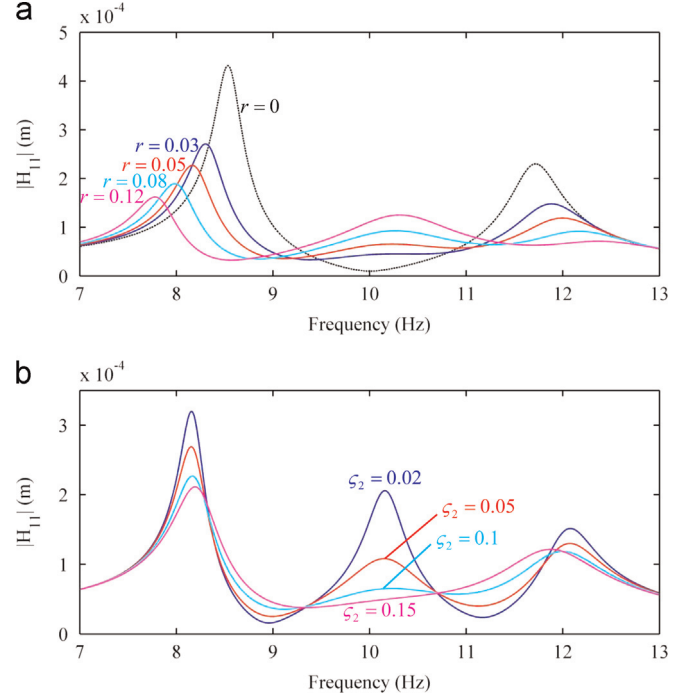


**Fig. 4.** FRFs of the mass  $m$  with  $r=s$  and  $\zeta = \zeta_1 = 0.02$ : (a)  $\zeta_2 = 0.1$  and different  $r$  values and (b)  $r = 0.05$  and different  $\zeta_2$  values.

displacement of the plate. The Young's modulus, density, Poisson's ratio and flexural rigidity of the plate are denoted by  $E$ ,  $\rho$ ,  $\nu$  and  $D$ , respectively. The variation of kinetic energy  $\delta T$  of the plate is

$$\delta T = \int_{-a}^a \int_{-b}^b (-\rho h \dot{w} \delta w) dx dy \quad (7)$$

The variation of elastic energy  $\delta \Pi$  of the plate can be represented as

$$\begin{aligned} \delta \Pi &= \int_{-a}^a \int_{-b}^b \int_{-h/2}^{h/2} (\sigma_{11} \delta \varepsilon_{11} + \sigma_{22} \delta \varepsilon_{22} + \sigma_{12} \delta \varepsilon_{12}) dz dx dy \\ &= \int_{-a}^a \int_{-b}^b \int_{-h/2}^{h/2} (-\sigma_{11} z \delta w_{xx} - \sigma_{22} z \delta w_{yy} - 2\sigma_{12} z \delta w_{xy}) dz dx dy \\ &= \int_{-a}^a \int_{-b}^b (-M_1 \delta w_{xx} - M_2 \delta w_{yy} - 2M_6 \delta w_{xy}) dx dy \\ &= \int_{-a}^a \int_{-b}^b (-M_{1xx} \delta w - M_{2yy} \delta w - 2M_{6xy} \delta w) dx dy \\ &\quad + \int_{-b}^b \left\{ [-M_1 \delta w_x + (M_{1x} + M_{6y}) \delta w - M_6 \delta w_y]_{x=-a}^{x=0^-} \right. \\ &\quad \left. + [-M_1 \delta w_x + (M_{1x} + M_{6y}) \delta w - M_6 \delta w_y]_{x=0^+}^{x=a} \right\} dy \\ &\quad + \int_{-a}^a \left\{ [-M_2 \delta w_y + (M_{2y} + M_{6x}) \delta w - M_6 \delta w_x]_{y=-b}^{y=0^-} \right. \\ &\quad \left. + [-M_2 \delta w_y + (M_{2y} + M_{6x}) \delta w - M_6 \delta w_x]_{y=0^+}^{y=b} \right\} dx \end{aligned} \quad (8)$$

where  $\varepsilon_{11}$ ,  $\varepsilon_{22}$  and  $\varepsilon_{12}$  are the normal strain along  $x$ , normal strain along  $y$  and in-plane shear strain, respectively. The non-conservative virtual work done by the external forces to the plate is

$$\begin{aligned} \delta W_{nc} &= \int_{-b}^b [-M_1 \delta w_x + Q_1 \delta w - M_6 \delta w_y]_{x=-a}^{x=a} dy \\ &\quad + \int_{-a}^a [-M_2 \delta w_y + Q_2 \delta w - M_6 \delta w_x]_{y=-b}^{y=b} dx + k_1 (u_1 - w_0) \delta w_0 \\ &\quad (Q_1 \equiv M_{1x} + M_{6y}, Q_2 \equiv M_{2y} + M_{6x}) \end{aligned} \quad (9)$$

where  $Q_1$  and  $Q_2$  are the transverse shear force intensities on the  $yz$  and  $xz$  planes,  $w_0$  is the displacement of the plate's center

where  $m_1$  is attached. Substituting Eqs. (7)–(9) to the extended Hamilton principle yields

$$\begin{aligned}
 0 &= \int_0^t (\delta T - \delta I + \delta W_{nc}) dt \\
 &= \int_0^t \left\{ \int_{-a}^a \int_{-b}^b (-\rho h \dot{w} + M_{1xx} + M_{2yy} + 2M_{6xy} \right. \\
 &\quad \left. + [\tilde{Q} + k_1(u_1 - w_0)] \delta(x, y) \right\} \delta w dx dy \Bigg|_0^t \\
 \tilde{Q} &\equiv (Q_1^x = \varepsilon_1/2 - Q_1^y = -\varepsilon_1/2) \varepsilon_2 + (Q_2^y = \varepsilon_2/2 - Q_2^x = -\varepsilon_2/2) \varepsilon_1, \quad \varepsilon_1, \varepsilon_2 \approx 0
 \end{aligned} \quad (10)$$

where  $\delta(x, y)$  is a 2D Dirac delta function, and  $\tilde{Q}$  accounts for the discontinuity of the internal transverse shear force at where  $m_1$  is attached. Setting the coefficient of  $\delta w$  in Eq. (10) to zero yields the governing equation for the plate as

$$-\rho h \ddot{w} + M_{1xx} + M_{2yy} + 2M_{6xy} + [\tilde{Q} + k_1(u_1 - w_0)] \delta(x, y) = 0 \quad (11)$$

Integrating Eq. (11) over the plate and using the definitions of  $M_1$ ,  $M_2$ ,  $M_6$  and  $\tilde{Q}$  gives

$$\begin{aligned}
 \int_{-a}^a \int_{-b}^b (-\rho h \ddot{w}) dy dx - D \int_{-a}^a (w_{yyy} + w_{xyy})_{y=-b}^{y=b} dx \\
 - D \int_{-b}^b (w_{xxx} + w_{xyy})_{x=-a}^{x=a} dy + k_1(u_1 - w_0) = 0
 \end{aligned} \quad (12)$$

Note that  $\tilde{Q}$  is canceled out after the integration. Eq. (12) can be interpreted as a rigid body moving with an acceleration averaged over its area and subject to transverse shear forces on its four edges and a concentrated force from the primary vibration absorber  $m_1$  at its center. In other words, the working unit in Fig. 5 can be treated as a dynamically equivalent 3-DOF system. The governing equations for the primary and secondary vibration absorbers  $m_1$  and  $m_2$  can be obtained by using Newton's second law as

$$m_1 \ddot{u}_1 - k_1 w_0 + (k_1 + k_2) u_1 - k_2 u_2 = 0 \quad (13)$$

$$m_2 \ddot{u}_2 - k_2 u_1 + k_2 u_2 = 0 \quad (14)$$

If a single-frequency harmonic wave propagates in an infinite metamaterial plate made of many of the working unit shown in Fig. 5, the plate's displacement  $w(x, y, t)$ , and the primary and secondary absorbers' displacements  $u_1(t)$  and  $u_2(t)$  can be represented as

$$w = p e^{i(\alpha x + \beta y - \omega t)}, \quad u_1 = q e^{-j\omega t}, \quad u_2 = r e^{-j\omega t} \quad (15)$$

where  $\alpha$  and  $\beta$  are the wavenumbers along  $x$  and  $y$  directions,  $\omega$  is the wave frequency, and  $p$ ,  $q$  and  $r$  are the vibration amplitudes. Substituting Eq. (15) into Eqs. (12)–(14) and rewriting the results in matrix form yields

$$\left[ \left\{ \frac{\sin(\alpha a) \sin(\beta b)}{\alpha \beta} \left[ \frac{4\rho h \omega^2 - 4D(\alpha^2 + \beta^2)^2}{4D(\alpha^2 + \beta^2)^2} - k_1 \right] \right\} \right. \\
 \left. k_1 0 k_1 m_1 \omega^2 - k_1 - k_2 k_2 0 k_2 m_2 \omega^2 - k_2 \right] \begin{Bmatrix} p \\ q \\ r \end{Bmatrix} = 0 \quad (16)$$

Eq. (16) is essentially an eigenvalue problem. The relation between  $\omega$  and  $\alpha$  and  $\beta$  can be found by setting the determinant of the matrix in Eq. (16) to zero. Corresponding to each pair of  $\alpha$  and  $\beta$ , there are three real and positive solutions for  $\omega$ . The parameters of the working unit for dispersion analysis are chosen to be consistent with parameters used in the following frequency response analysis so that stopbands from two analyses can be

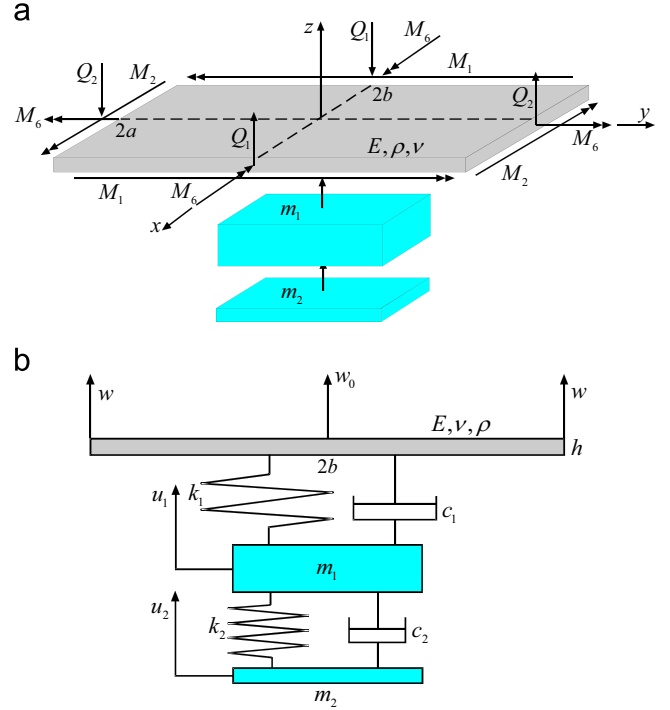


Fig. 5. A 3-DOF model of a working unit of the metamaterial plate.

compared.

Lengths :  $2a = 0.125\text{m}$ ,  $2b = 0.125\text{m}$ ,

Plate thickness :  $h = 15\text{ mm}$

Young's moduls :  $E = 72.4\text{ GPa}$ ,

Poisson's ratio :  $\nu = 0.33$ ,

Mass density :  $\rho = 2800\text{kg/m}^3$

Attached masses :  $m_1 = 65.6\text{ g}$ ,  $m_2 = 0.05m_1 = 3.3\text{ g}$ ,

$\omega_{n1} = \omega_{n2} = 800\text{ Hz}$  (17)

Fig. 6(a) shows a perspective view of the dispersion surfaces in a selected zone having  $0 < \alpha < 20$  and  $0 < \beta < 20$ . Because three real and positive values of  $\omega$  can be obtained for each pair of  $\alpha$  and  $\beta$ , there are three dispersion surfaces in Fig. 6(a). If no vibration absorbers are attached to the plate, there is only one dispersion surface and the plate is self-dispersive because the speed of a harmonic wave propagating in it changes with the wave frequency. In order to clearly show the two stopbands among the three dispersion surfaces, the frequency value along the four edges of each dispersion surface (e.g.,  $M - \Gamma - \Pi - X - M$  of the upper dispersion surface in Fig. 6(a)) is traced and plotted in Fig. 6(b). The dotted black curve in Fig. 6(b) is of an isotropic plate without absorbers (i.e.,  $m_1 = m_2 = 0$ ). The two stopbands among the three dispersion curves are 712.9–737.6 Hz and 891.7–912.1 Hz if the resonant frequency of the primary and secondary vibration absorbers is tuned to be  $\omega_{n1} = \omega_{n2} = 800\text{ Hz}$ .

Fig. 7 shows how the two stopbands change with different parameters of the working unit. The black dotted line is the referential case using the parameter values in Eq. (17). The red line shows the result with the working unit's side lengths being reduced (i.e., less weight) to  $2a = 2b = 0.125\text{ m}$ . The lower bounds of both stopbands remain almost the same but the upper bounds of both stopbands move upward, and hence the stopbands become wider. The blue line shows the result with  $m_1$  being reduced to  $m_1 = 0.025\text{ kg}$ . The lower bounds of both stopbands move upward and the upper bounds move downward, and hence the stopbands become narrower. The cyan line shows the result with  $h$  being increased to 20 mm. The upper and lower bounds of both

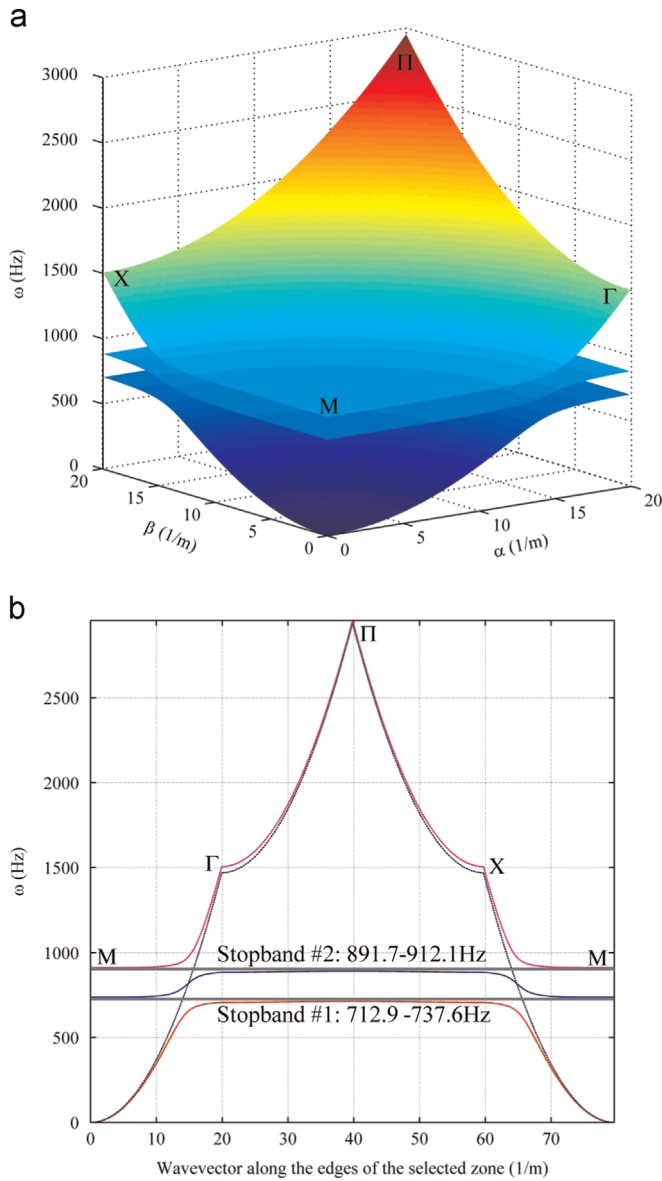


**Fig. 6.** Dispersion surfaces and stopbands of the metamaterial plate: (a) dispersion surfaces and (b) stopbands.

stopbands move upward and hence the bandwidth of each stopband has no significant change. These results show that the most significant way of increasing each stopband’s bandwidth is to increase the mass ratio  $m_1/(4abh\rho)$ .

#### 4. Frequency response analysis of multi-stopband metamaterial plates

In order to include the influences of boundary conditions and loading on a metamaterial plate, we consider a multi-stopband metamaterial wall shown in Fig. 8(a), which has horizontal length  $L_a=5$  m and vertical length  $L_b=3$  m. The two vertical edges at  $x=0$  and  $5$  m (red stars in Fig. 8(b)) are hinged, and a harmonic force with amplitude of 100 kN is applied at the second node (green star in Fig. 8(b)) from the left end of the centerline. The isotropic plate is modeled with  $40 \times 24$  first-order shear-deformable rectangular plate elements with conforming behavior along element edges. The magenta dots at the element nodes represent the multi-frequency absorbers. There are no absorbers on the

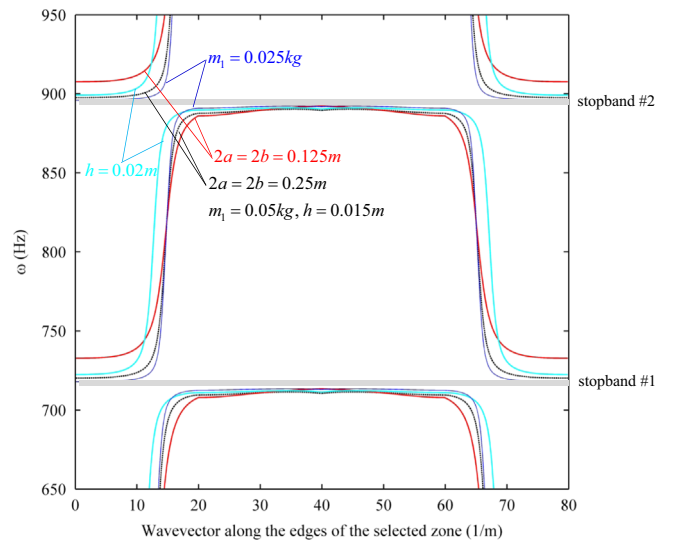


**Fig. 7.** Variations of stopbands under different values of parameters. (For interpretation of the references to color in this figure, the reader is referred to the web version of this article.)

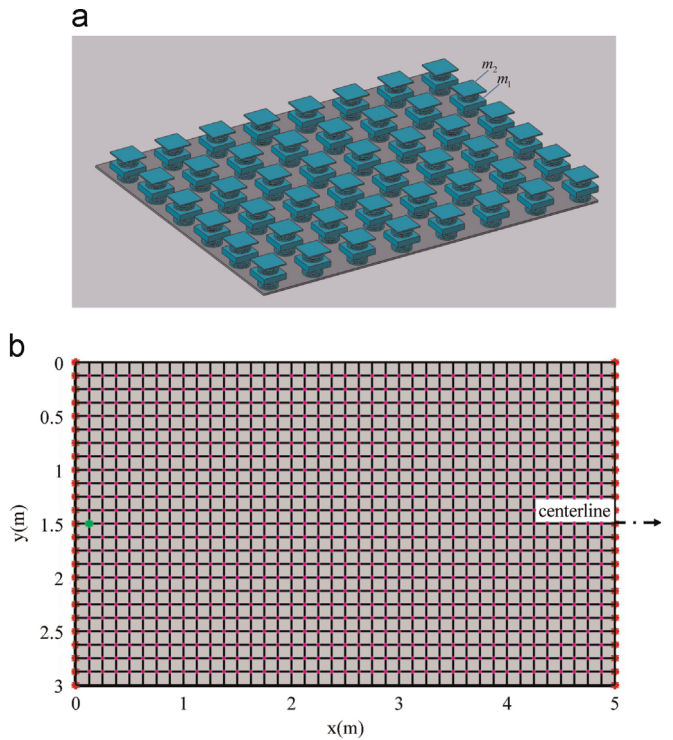


**Fig. 8.** A multi-stopband metamaterial wall: (a) 3D view and (b) finite element discretization. (For interpretation of the references to color in this figure, the reader is referred to the web version of this article.)

hinged edges at  $x=0$  and  $5$  m and the free edges at  $y=0$  and  $3$  m. The physical properties and thickness of the plate are the same as the working unit analyzed in the dispersion analysis. The masses of each absorber are  $m_1=65.6$  g and  $m_2=0.05m_1$ , and the total absorber mass is 9.81% of the whole structure mass. The resonant frequencies of the primary and secondary absorbers are both set to be  $\omega_{n1}=\omega_{n2}=800$  Hz.

In order to quantify the vibration suppression performance of metamaterial plates, the difference between frequency response functions (FRFs) for metamaterial plates and isotropic plates is used. For example, the average FRF of the isotropic plate at  $x=0.5$   $L_a$  is calculated and then the average FRF of the metamaterial plate

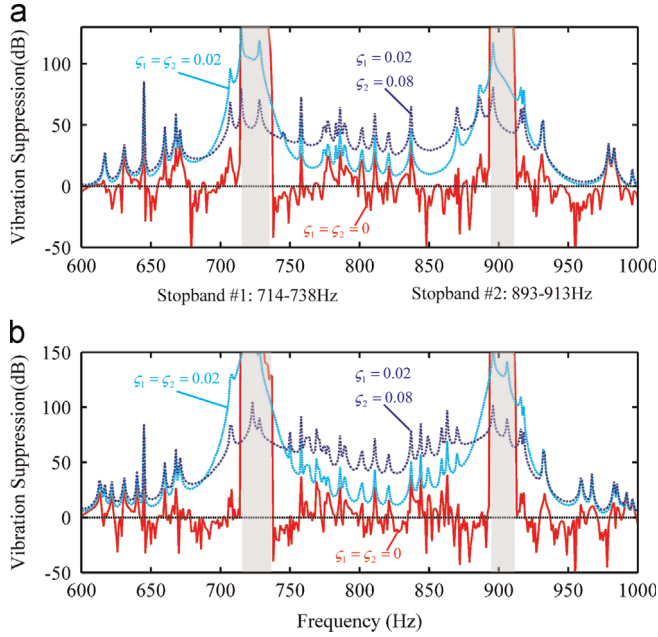


**Fig. 9.** Vibration suppression with different damping ratios for absorbers: (a) average vibration suppression at  $x=2.5$  m and (b) average vibration suppression at  $x=4$  m. (For interpretation of the references to color in this figure, the reader is referred to the web version of this article.)

at the same locations is subtracted from the FRF of the isotropic plate. The resultant FRF represents how much vibration is suppressed after adding the vibration absorbers to the isotropic plates. Therefore, a vibration suppression function  $S$  can be defined as

$$S = 20 \log_{10}(\bar{w}) - 20 \log_{10}(\bar{W}) \quad (18)$$

where  $\bar{w}$  and  $\bar{W}$  are the average displacement on the same location of the plate (e.g.,  $x=0.5L_a$  and  $x=0.8L_a$ ) before and after attaching the vibration absorbers.

Fig. 9(a) and (b) shows the vibration suppression function at  $x=0.5L_a$  and  $x=0.8L_a$ , respectively. The horizontal black dash lines in Fig. 9(a) and (b) represent that no influence is introduced after adding the vibration absorbers, and any curves above this line represent vibration reduction. The damping ratios of the primary and secondary absorbers are denoted with  $\zeta_1$  and  $\zeta_2$ , and the red solid lines represent the vibration suppression function with  $\zeta_1 = \zeta_2 = 0$ . With zero damping, two stopbands where vibration suppression abruptly increases, are shown by the gray bands. These two stopbands, with ranges 714–738 Hz and 893–913 Hz, are slightly different from those in the dispersion analysis (712.9–737.6 Hz and 891.7–912.1 Hz in Fig. 6) because boundary conditions and loading are not considered in dispersion analysis. The red solid lines show that although vibration in the stopbands are well suppressed, vibration under frequencies outside of the stopbands is not properly reduced, and at some frequencies even increased (curves under the horizontal back dash line). The cyan dash-dot lines in Fig. 9 represent the vibration suppression function with  $\zeta_1 = \zeta_2 = 0.02$ . Although two stopbands are widened by non-zero damping ratios, the two stopbands are not combined into a continuous broad stopband. The blue dash lines represent the vibration suppression function with  $\zeta_1 = 0.02$  and  $\zeta_2 = 0.08$ . The low damping in the primary absorber ( $\zeta_1$ ) allows for quick response to transient excitation and the high damping in the secondary absorber ( $\zeta_2$ ) helps suppress the steady-state vibration. The blue dash lines show that the two stopbands are combined into a broad continuous stopband and the vibration within 600–1000 Hz are well suppressed. Figs. 10–12 show the plate's steady-state operational deflection shapes (ODSs) under excitation

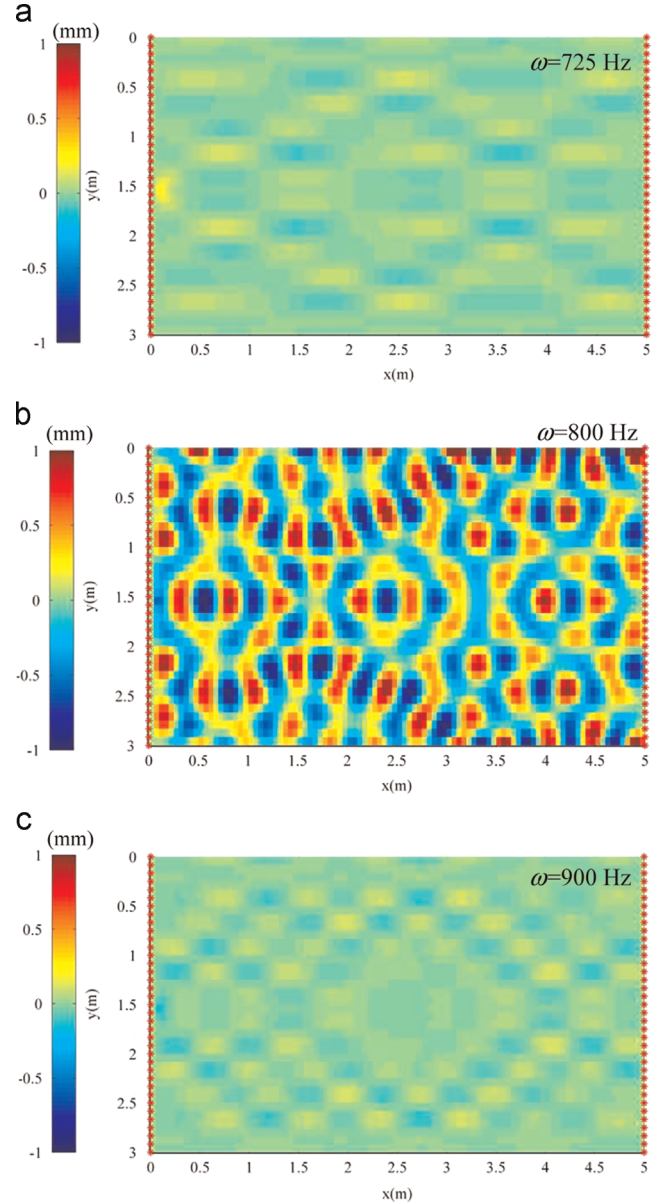


**Fig. 10.** Steady-state ODSs with  $\zeta_1 = \zeta_2 = 0$ : (a)  $\omega=725$  Hz, (b)  $\omega=800$  Hz, and (c)  $\omega=900$  Hz.

frequencies at 725 Hz (in the first stopband), 800 Hz (between the two stopbands) and 900 Hz (in the second stopband). No damping is used in Fig. 11,  $\zeta_1 = \zeta_2 = 0.02$  is used in Fig. 12, and  $\zeta_1 = 0.02$  and  $\zeta_2 = 0.08$  is used in Fig. 12. When the excitation frequency falls into the stopbands, waves cannot propagate through for all three cases. However, significant vibration suppression between the two stopbands is only observed when large damping is used for the secondary vibration absorbers, as shown by Figs. 10(b) and 12(b).

## 5. Transient analysis of multi-stopband metamaterial plates

Because stresses in a structure during the transient period right after loading are often larger than those in steady states, structural failure often occurs during the transient period. Although frequency response analysis (FRA) shown in Section 4 can reveal the performance of the metamaterial wall at steady states, how the metamaterial wall behaves before the steady state is also crucial

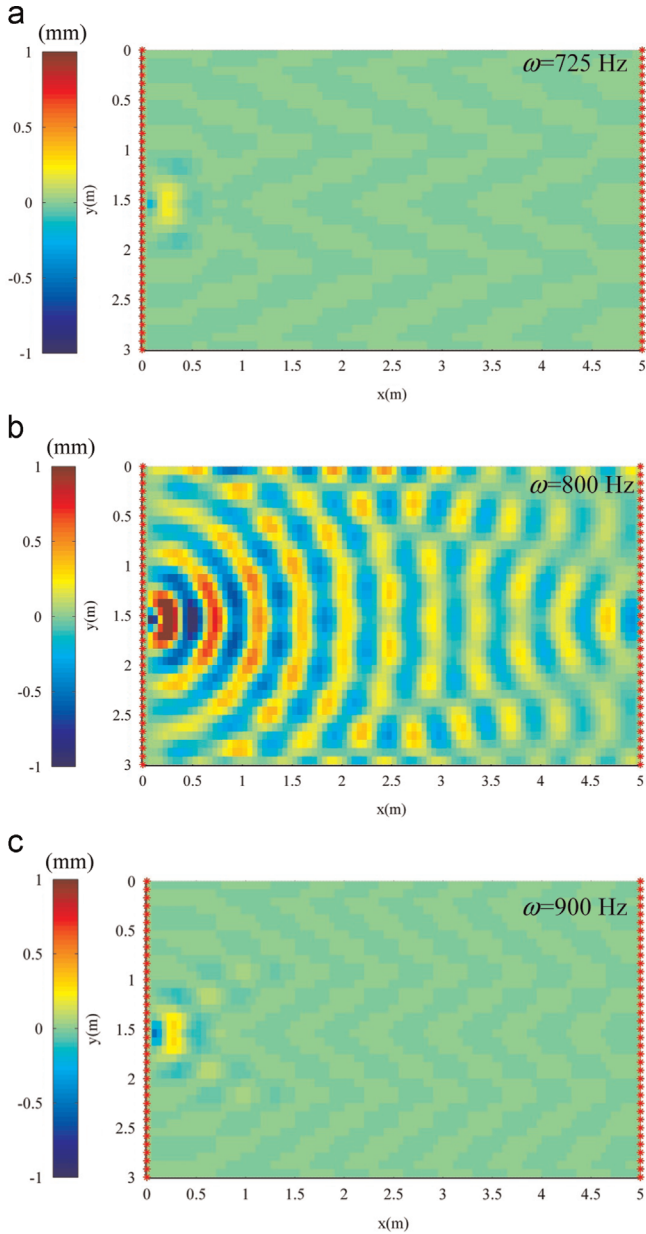


Fig. 11. Steady-state ODSs with  $\zeta_1 = \zeta_2 = 0.02$ : (a)  $\omega = 725$  Hz, (b)  $\omega = 800$  Hz, and (c)  $\omega = 900$  Hz.

for design and needs to be examined by performing direct numerical integration of the finite-element equations. Figs. 13–15 show the transient responses, operational deflection shapes (ODSs) and distributions of the transverse shear force intensity  $Q_1$  of the metamaterial wall with  $\zeta_1 = 0.02$  and  $\zeta_2 = 0.08$  under different excitation frequencies 725 Hz, 800 Hz and 900 Hz, respectively. The ODSs are obtained at the end of the numerical integration.

The red, green and blue lines in Fig. 13(a) represent the transient vibrations of nodes at  $x = 1$  m, 2.5 m and 4 m on the centerline ( $y = 1.5$  m). It takes about 0.269 s (195 excitation periods) for the structure to reach its steady state. Fig. 13(b) shows that both the plate and absorbers have almost zero vibration amplitudes beyond  $x > 2.5$  m. The blue line, black lines and red lines in Fig. 13 (b) represent the ODSs of the plate, primary absorbers, and secondary absorbers, respectively. When the excitation frequency falls within the first stopband (e.g.,  $\omega = 725$  Hz), the primary and secondary absorbers move in phase and there is a  $90^\circ$  phase angle

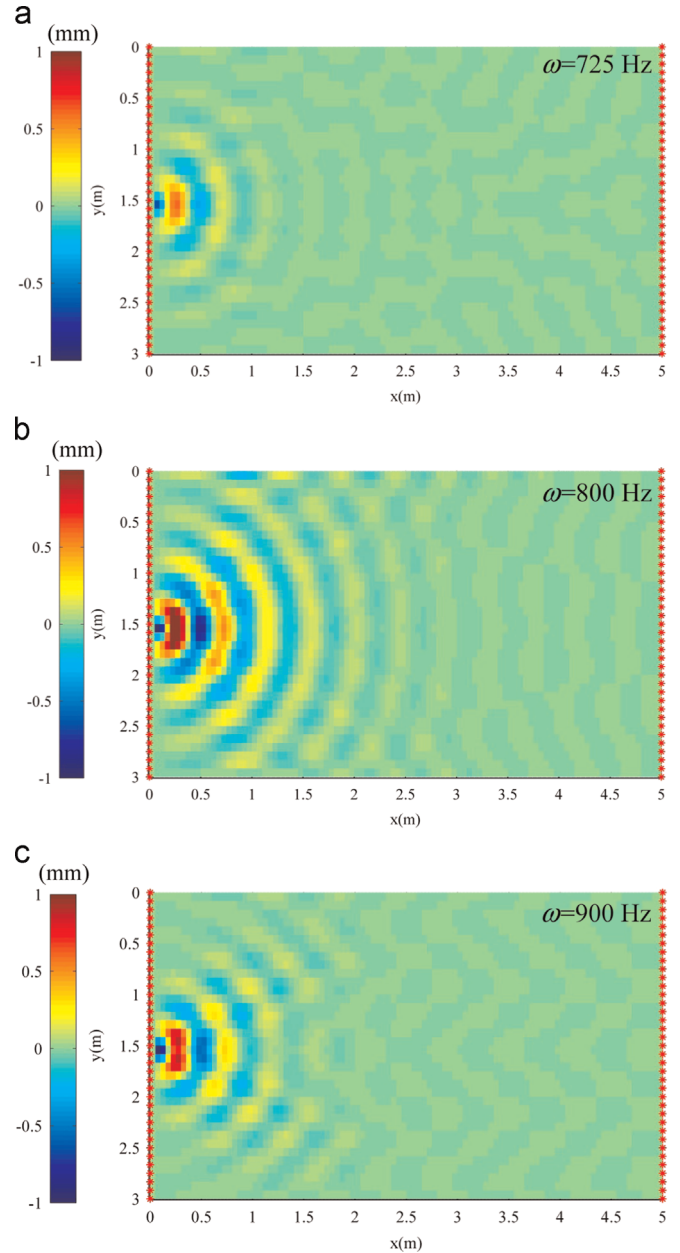
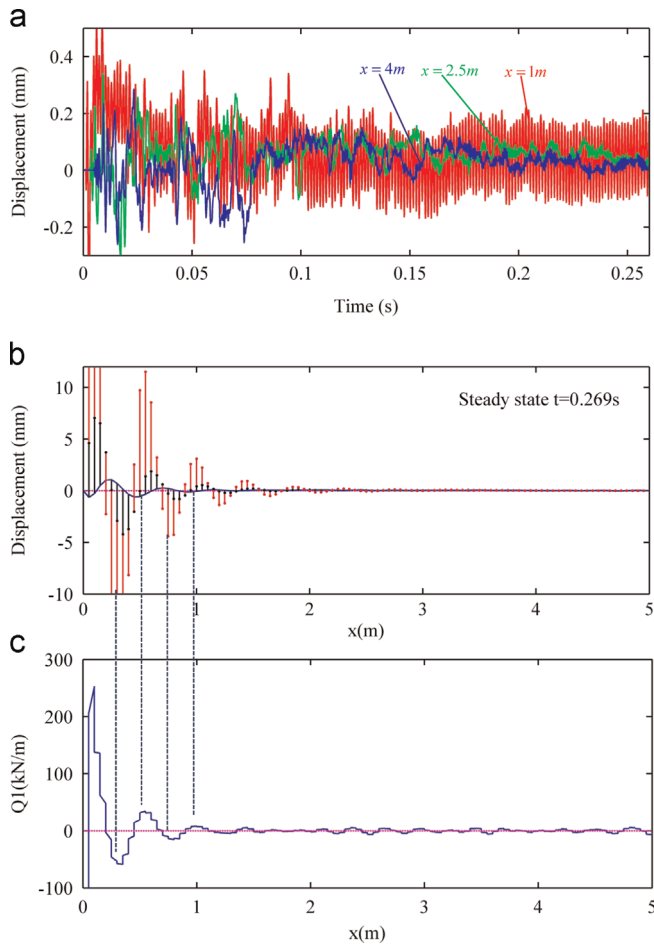


Fig. 12. Steady-state ODSs with  $\zeta_1 = 0.02$  and  $\zeta_2 = 0.08$ : (a)  $\omega = 725$  Hz, (b)  $\omega = 800$  Hz, and (c)  $\omega = 900$  Hz.

between the absorbers and the plate. In other words, the plate and absorbers move in a mixed mode consisting of optical and acoustic modes. Fig. 13(c) shows the transverse shear force intensity along the centerline. The first peak is due to the concentrated excitation force. The corresponding relations between the other four extreme values in Fig. 13(c) and the extreme values of the plate's ODS in Fig. 13(b) are indicated by the dash lines. It is obvious that large values of  $Q_1$  happen around where the plate has large curvatures and straighten the plate to stop/attenuate wave propagation. This is the actual working mechanism of this metamaterial plate based on vibration absorbers.

Results in Fig. 14 are similar to those in Fig. 13 but the excitation frequency is set at 800 Hz. Fig. 14(a) shows that it takes about 0.196 s (157 excitation periods) for the structure to reach its steady state. Fig. 14(b) shows that the plate (blue line) and secondary vibration absorbers (red dots) work in an optical mode (i.e., out of phase by  $180^\circ$ ) but the primary vibration absorbers work in a



**Fig. 13.** Transient analysis under  $\omega = 725$  Hz: (a) vibration of nodes at  $x = 1$  m, 2.5 m and 4 m on the centerline, (b) ODSs from direct numerical integration, and (c) distribution of shear intensity  $Q_1$  along centerline. (For interpretation of the references to color in this figure, the reader is referred to the web version of this article.)

mixed mode. Fig. 14(c) shows that the extreme shear force values created by the primary absorbers' mixed-mode vibrations straighten the isotropic plate and stop the wave from propagating forward. Results in Fig. 15 are under an excitation frequency  $\omega = 900$  Hz (in the second stopband). Fig. 15(a) shows that it takes 0.196 s (176 excitation period) to reach a steady state. Fig. 15 (b) shows that the primary and secondary vibration absorbers are  $180^\circ$  out of phase. The plate and primary absorbers (black dots) work in an optical mode and the plate and secondary absorbers work in a mixed mode. Although  $\omega = 800$  Hz is not within one of the two stopbands, Fig. 14(b) shows that the excited wave cannot propagate forward because the excitation energy is transferred into the absorbers and damped out by the high damping of the secondary absorbers.

## 6. Sensitivity analysis

In the above analyses, the resonant frequencies of the primary and secondary vibration absorbers are ideally set to 800 Hz but this ideal scenario is not easy to realize in real design process. Taking the mass–spring type vibration absorbers as an example, even if the attached mass is accurately weighed and the spring constants are carefully calibrated, error will probably be introduced in the assembly processes, which include welding, gluing or bolting. Because error is not avoidable in application, how

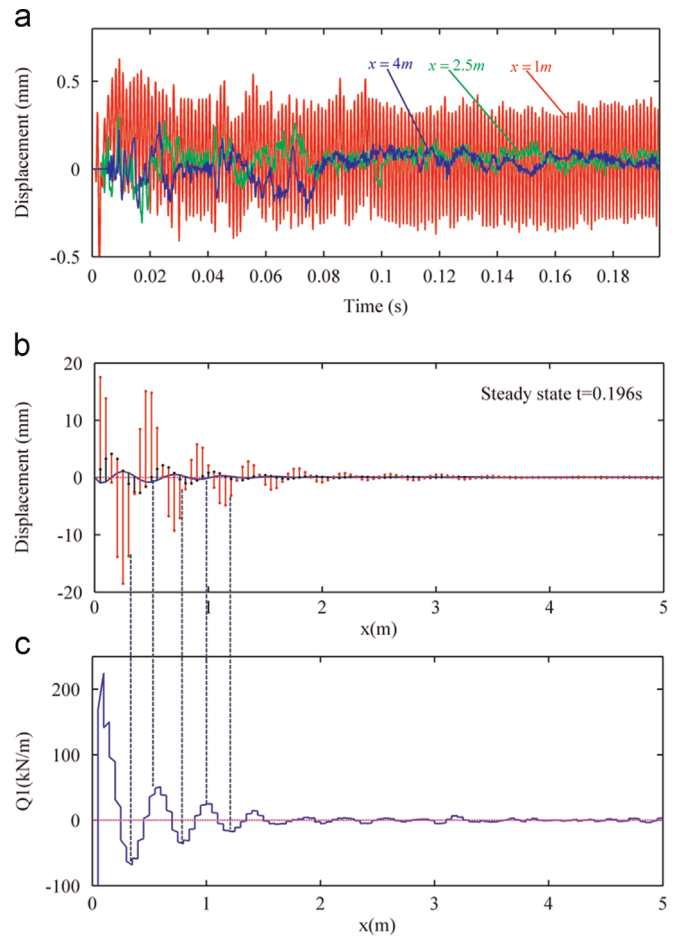


**Fig. 14.** Transient analysis under  $\omega = 800$  Hz: (a) vibration of nodes at  $x = 1$  m, 2.5 m and 4 m on the centerline, (b) ODSs from direct numerical integration, and (c) distribution of shear intensity  $Q_1$  along centerline. (For interpretation of the references to color in this figure, the reader is referred to the web version of this article.)

sensitively the metamaterial plates respond to the error is of great interest to us.

In the sensitivity analysis, the resonant frequencies of the primary and secondary vibration absorbers are assumed to obey normal distributions with mean 800 Hz and different standard deviations. Fig. 16(a) and (b) show the average vibration suppression function of metamaterial plates at  $x = 2.5$  m and  $x = 4$  m. Based on the former frequency response analysis, optimal damping ratios  $\zeta_1 = 0.02$  and  $\zeta_2 = 0.08$  are used. The vibration suppression function for metamaterial plates with absorber resonant frequency distribution  $N(800, 0)$  Hz,  $N(800, 80^2)$  Hz and  $N(800, 160^2)$  Hz are plotted with red solid lines, cyan dash lines and blue dash-dot lines, respectively. Large sensitivity is observed at two stopband regions (near 725 Hz and 900 Hz) and sensitivity near 800 Hz is almost zero. It's also interesting to note that non-uniform absorber natural frequencies improve the vibration suppression function at 600–670 Hz and 925–1000 Hz. In conclusion, the performance of metamaterial plates seems not quite sensitive to the error introduced into the absorber natural frequencies. However, the sensitivity at two stopband regions is relatively large, and extra attention should be paid if excitation frequencies are in the two regions.

## 7. Conclusions

This paper investigates and reveals the working mechanism and provides design guidelines for multi-stopband metamaterial

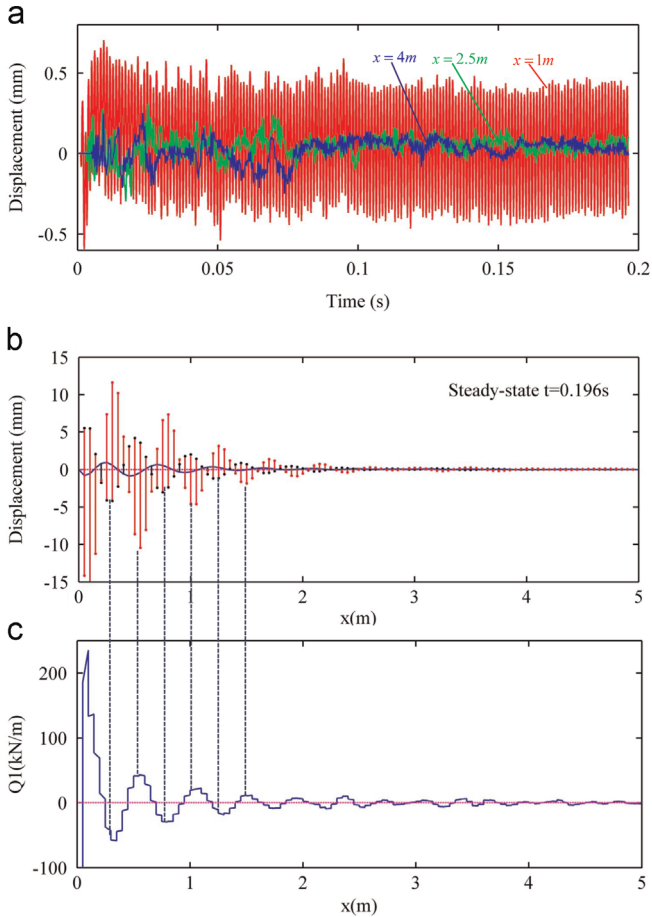


**Fig. 15.** Transient analysis under  $\omega=900$  Hz: (a) vibration of nodes at  $x=1$  m, 2.5 m and 4 m on the centerline, (b) ODSs from direct numerical integration, and (c) distribution of shear intensity  $Q_1$  along centerline.

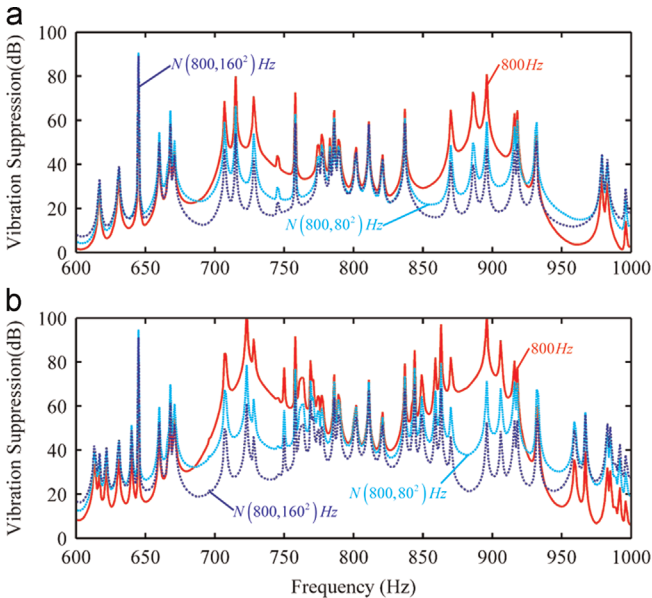


**Fig. 16.** Vibration suppression for metamaterial plates with absorber natural frequencies at random distributions  $N(800, 0)$ ,  $N(800, 80^2)$  and  $N(800, 160^2)$ : (a) average vibration suppression at  $x=2.5$  m and (b) average vibration suppression at  $x=4$  m. (For interpretation of the references to color in this figure, the reader is referred to the web version of this article.)

plates with two-mass vibration absorbers for elastic wave absorption and vibration suppression. Dispersion analysis of a working unit and frequency response analysis and transient analysis by direct integration of a full-size finite-element model with boundary conditions are conducted to investigate the stopband effect. Two stopbands are generated at the two sides of the absorbers' resonant frequency. The multi-stopband metamaterial plate is shown to be based on the concept of traditional multi-frequency vibration absorbers. The local resonant vibrations of the vibration absorbers generate inertial forces to straighten the plate's bending and attenuate/stop wave propagation. The low damping in the primary absorber allows the excitation energy be quickly transferred into the absorbers, and the high damping in the secondary absorber combines the two stopbands into a broad stopband and damps out the excitation energy. Sensitivity analysis shows that relatively large sensitivity is found at the two stopband regions.

**References**

- [1] Veselago VG. The electrodynamics of substances with simultaneously negative values of permittivity and permeability. *Sov Phys Usp* 1968;10:509–14.
- [2] Pendry JB. Negative refraction makes a perfect lens. *Phys Rev Lett* 2000;85:3966–9.
- [3] Alù A, Engheta N. Plasmonic and metamaterial cloaking: physical mechanisms and potentials. *J Opt A: Pure Appl Opt* 2008;10:093002.
- [4] Schurig D, Mock JJ, Justice BJ, Cummer SA, Pendry JB, Starr AF, et al. Metamaterial electromagnetic cloak at microwave frequencies. *Science* 2006;314:977–80.
- [5] Seddon N, Bearpark T. Observation of the inverse Doppler effect. *Science* 2003;302:1537–40.
- [6] Fok L, Ambati M, Zhang X. Acoustic metamaterials. *MRS Bull* 2008;33:931–4.
- [7] Pai PF. Metamaterial-based broadband elastic wave absorber. *J Intell Mater Syst Struct* 2010;21:517–28.
- [8] Pai PF, Peng H, Jiang S. Acoustic metamaterial beams based on multi-frequency vibration absorbers. *Int J Mech Sci* 2014;79:195–205.
- [9] Sun H, Du X, Pai PF. Theory of metamaterial beams for broadband vibration absorption. *J Intell Mater Syst Struct* 2010.
- [10] Peng H, Frank Pai P. Acoustic metamaterial plates for elastic wave absorption and structural vibration suppression. *Int J Mech Sci* 2014;89:350–61.
- [11] Zhang S, Park Y-S, Li J, Lu X, Zhang W, Zhang X. Negative refractive index in chiral metamaterials. *Phys Rev Lett* 2009;102.
- [12] Zhang S. Acoustic metamaterial design and applications. Mechanical engineering, University of Illinois at Urbana-Champaign; 2010.
- [13] Zhu R, Huang GL, Huang HH, Sun CT. Experimental and numerical study of guided wave propagation in a thin metamaterial plate. *Phys Lett A* 2011;375:2863–7.
- [14] Zhu R, Liu XN, Hu GK, Sun CT, Huang GL. A chiral elastic metamaterial beam for broadband vibration suppression. *J Sound Vib* 2014;333:2759–73.
- [15] Bozorgnia Y, Bertero VV. Earthquake engineering: from engineering seismology to performance-based engineering. CRC Press; 2004.
- [16] Kim S-H, Das MP. Seismic waveguide of metamaterials. *Mod Phys Lett B* 2012;26:1250105.
- [17] Brûlé S, Javelaud EH, Enoch S, Guenneau S. Experiments on seismic metamaterials: molding surface waves. *Phys Rev Lett* 2014;112.
- [18] Deymier PA. Acoustic metamaterials and phononic crystals. Berlin Heidelberg: Springer; 2013.
- [19] Lu M-H, Feng L, Chen Y-F. Phononic crystals and acoustic metamaterials. *Mater Today* 2009;12:34–42.
- [20] Sigalas MM, Economou EN. Elastic waves in plates with periodically placed inclusions. *J Appl Phys* 1994;75:2845–50.
- [21] Psarobas IE, Stefanou N, Modinos A. Scattering of elastic waves by periodic arrays of spherical bodies. *Phys Rev B* 2000;62:278–91.
- [22] Hsu J-C, Wu T-T. Lamb waves in binary locally resonant phononic plates with two-dimensional lattices. *Appl Phys Lett* 2007;90:201904.
- [23] Sigalas M, Economou EN. Band structure of elastic waves in two dimensional systems. *Solid State Commun* 1993;86:141–3.
- [24] Yang S, Page JH, Liu Z, Cowan ML, Chan CT, Sheng P. Focusing of sound in a 3D phononic crystal. *Phys Rev Lett* 2004;93:024301.
- [25] Goffaux C, Sánchez-Dehesa J, Yeyati AL, Lambin P, Khelif A, Vasseur JO, et al. Evidence of Fano-like interference phenomena in locally resonant materials. *Phys Rev Lett* 2002;88:225502.
- [26] Zhu R, Huang GL, Hu GK. Effective dynamic properties and multi-resonant design of acoustic metamaterials. *J Vib Acoust* 2012;134:031006.
- [27] Liu Z, Zhang X, Mao Y, Zhu YY, Yang Z, Chan CT, et al. Locally resonant sonic. *Mater Sci* 2000;289:1734–6.
- [28] Ho KM, Cheng CK, Yang Z, Zhang XX, Sheng P. Broadband locally resonant sonic shields. *Appl Phys Lett* 2003;83:5566.

- [29] Ding Y, Liu Z, Qiu C, Shi J. Metamaterial with simultaneously negative bulk modulus and mass density. *Phys Rev Lett* 2007;99.
- [30] Li J, Chan CT. Double-negative acoustic metamaterial. *Phys Rev E* 2004;70.
- [31] Jensen JS. Phononic band gaps and vibrations in one- and two-dimensional mass-spring structures. *J Sound Vib* 2003;266:1053–78.
- [32] Martinsson PG, Movchan AB. Vibrations of lattice structures and phononic band gaps. *Q J Mech Appl Math* 2003;56:45–64.
- [33] Willis JR, Milton GW. On modifications of Newton's second law and linear continuum elastodynamics. *Proc R Soc A: Math Phys Eng Sci* 2007;463:855–80.
- [34] Yao S, Zhou X, Hu G. Experimental study on negative effective mass in a 1D mass-spring system. *New J Phys* 2008;10:043020.
- [35] Cheng Y, Xu JY, Liu XJ. One-dimensional structured ultrasonic metamaterials with simultaneously negative dynamic density and modulus. *Phys Rev B* 2008;77:045134.
- [36] Cheng Y, Xu JY, Liu XJ. Broad forbidden bands in parallel-coupled locally resonant ultrasonic metamaterials. *Appl Phys Lett* 2008;92:051913.
- [37] Wu T-T, Huang Z-G, Tsai T-C, Wu T-C. Evidence of complete band gap and resonances in a plate with periodic stubbed surface. *Appl Phys Lett* 2008;93:111902.
- [38] Oudich M, Li Y, Assouar BM, Hou Z. A sonic band gap based on the locally resonant phononic plates with stubs. *New J Phys* 2010;12:083049.
- [39] Zhu R, Huang HH, Huang GL, Sun CT. Microstructure continuum modeling of an elastic metamaterial. *Int J Eng Sci* 2011;49:1477–85.
- [40] Zhu R, Liu XN, Hu GK, Yuan FG, Huang GL. Microstructural designs of plate-type elastic metamaterial and their potential applications: a review. *Int J Smart Nano Mater* 2015;6:14–40.
- [41] Pai PF. Highly flexible structures: modeling, computation, and experimentation. American Institute of Aeronautics and Astronautics; 2007.